

Enhancing p-d hybridization via synergistic regulation of spatial and energetic orbital overlaps in Ba-doped $LaNiO_3$ epitaxial films for oxygen evolution activity

Yingjia Li(李莹嘉), Xiang Xu(徐翔), Xiaoyu Qiu(邱晓宇), Jie Tu(涂杰), Zijian Chen(陈子健), Yujie Zhou(周雨洁), Zhao Guan(关赵), Youyuan Zhang(张友圆), Wen-Yi Tong(童文旖), Shaohui Xu(徐少辉), Ni Zhong(钟妮), Pinghua Xiang(向平华), Chun-Gang Duan(段纯刚), and Binbin Chen(陈斌斌)

Citation : Chin. Phys. B, 2025, 34 (**5**): 057101. DOI: 10.1088/1674-1056/adc7f8
http://cpb.iphy.ac.cn; http://iopscience.iop.org/cpb

What follows is a list of articles you may be interested in

Structural, electronic and magnetic properties of Fe-doped strontium ruthenates

Nan Liu(刘楠), Xiao-Chao Wang(王晓超), and Liang Si(司良)
Chin. Phys. B, 2023, 32 (**11**): 117101. DOI: 10.1088/1674-1056/ad0112

Single crystal growth and electronic structure of Rh-doped $Sr_3Ir_2O_7$

Bingqian Wang(王冰倩), Shuting Peng(彭舒婷), Zhipeng Ou(欧志鹏), Yuchen Wang(王宇晨), Muhammad Waqas, Yang Luo(罗洋), Zhiyuan Wei(魏志远), Linwei Huai(淮琳崴), Jianchang Shen(沈建昌), Yu Miao(缪宇), Xiupeng Sun(孙秀鹏), Yuewei Yin(殷月伟), and Junfeng He(何俊峰)
Chin. Phys. B, 2023, 32 (**8**): 087108. DOI: 10.1088/1674-1056/acd7d5

Highly anisotropic Dirac fermion and spin transportproperties in Cu-graphane

Chao Wu(吴超), Lichuan Zhang(张礼川), Lin Xia(夏霖), Dong Hao(郝东), Shiqi Li(李仕琪), Lizhi Zhang(张礼智), Yuee Xie(谢月娥), and Yuanping Chen(陈元平)
Chin. Phys. B, 2023, 32 (**8**): 087104. DOI: 10.1088/1674-1056/accff1

Flat band in hole-doped transition metal dichalcogenide observed by angle-resolved photoemission spectroscopy

Zilu Wang(王子禄), Haoyu Dong(董皓宇), Weichang Zhou(周伟昌), Zhihai Cheng(程志海), and Shancai Wang(王善才)
Chin. Phys. B, 2023, 32 (**6**): 067103. DOI: 10.1088/1674-1056/acc7f9

Formation of quaternary all-d-metal Heusler alloy by Co doping fcc type Ni_2MnV and mechanical grinding induced B2-fcc transformation

Lu Peng(彭璐), Qiangqiang Zhang(张强强), Na Wang(王娜), Zhonghao Xia(夏中昊), Yajiu Zhang(张亚九),Zhigang Wu(吴志刚), Enke Liu(刘恩克), and Zhuhong Liu(柳祝红)
Chin. Phys. B, 2023, 32 (**1**): 017102. DOI: 10.1088/1674-1056/ac5e94

RAPID COMMUNICATION

Enhancing p–d hybridization via synergistic regulation of spatial and energetic orbital overlaps in Ba-doped $LaNiO_3$ epitaxial films for oxygen evolution activity

Yingjia Li(李莹嘉), Xiang Xu(徐翔), Xiaoyu Qiu(邱晓宇), Jie Tu(涂杰), Zijian Chen(陈子健), Yujie Zhou(周雨洁), Zhao Guan(关赵), Youyuan Zhang(张友圆), Wen-Yi Tong(童文旖)†, Shaohui Xu(徐少辉), Ni Zhong(钟妮), Pinghua Xiang(向平华), Chun-Gang Duan(段纯刚), and Binbin Chen(陈斌斌)‡

Key Laboratory of Polar Materials and Devices (MOE) and Department of Electronics, East China Normal University, Shanghai 200241, *China*

(Received 27 February 2025; revised manuscript received 25 March 2025; accepted manuscript online 2 April 2025)

The hybridization between oxygen 2p and transition-metal 3d states largely determines the electronic structure near the Fermi level and related functionalities of transition-metal oxides (TMOs). Considerable efforts have been made to manipulate the p–d hybridization in TMOs by tailoring the spatial orbital overlap via structural engineering. Here, we demonstrate enhanced p–d hybridization in Ba^{2+}-doped $LaNiO_3$ epitaxial films by simultaneously modifying both the spatial and energetic overlaps between the O-2p and Ni-3d orbitals. Combining x-ray absorption spectroscopy and first-principles calculations, we reveal that the enhanced hybridization stems from the synergistic effects of a reduced charge-transfer energy due to hole injection and an increased spatial orbital overlap due to straightening of Ni–O–Ni bonds. We further show that the enhanced p–d hybridization can be utilized to promote the oxygen evolution activity of $LaNiO_3$. This work sheds new insights into the fine-tuning of the electronic structures of TMOs for enhanced functionalities.

Keywords: transition-metal oxide, doping, p–d hybridization, orbital overlap, oxygen evolution activity

PACS: 61.72.–y, 71.20.Be, 75.25.Dk, 82.45.–h

DOI: 10.1088/1674-1056/adc7f8 **CSTR:** 32038.14.CPB.adc7f8

1. Introduction

In transition-metal oxides (TMOs), the hybridization between the p orbital of oxygen and the d orbital of the transition-metal ion plays a decisive role in the properties of the oxide, such as conductivity,[1,2] magnetism,[3,4] ferroelectricity,[5] catalytic properties,[6] etc. Generally, the p–d hybridization in TMOs is controlled by altering the spatial overlap between the two orbitals via engineering the bond angle and/or bond length. In perovskite oxides ABO_3, the B–O–B bond angle is related to the Goldschmidt tolerance factor t,

$$t = (r_A + r_O)/\sqrt{2}(r_B + r_O),$$

where r_A, r_B, and r_O represent the radii of the A, B, and oxygen ions, respectively.[7] Increasing t toward unity is expected to straighten the B–O–B bond angle and thus enhance p–d hybridization. This can be done by introducing larger ions at the A site via chemical substitution. In thin films, epitaxial strain has been commonly used for structural engineering.[8,9] Strain accommodation is complicated in ABO_3 films and is usually associated with distortions in both bond angle and bond length.[10] For instance, in-plane compressive strain tends to shorten the in-plane B–O bond length while simultaneously increasing the buckling of the in-plane B–O–B bonds. The two competing effects determine the p–d hybridization under strain. The B–O–B bond angle can also be modulated via the interfacial BO_6 oxygen octahedral coupling.[11] This type of geometric constraint effect is only effective within a few unit cells from the interface, providing another tool for controlling the p–d hybridization in ultrathin films.[12–14] On the other hand, p–d hybridization also depends on the charge transfer energy Δ, the energy cost of transferring an electron from the O-2p band to the transition metal d band. For early TMOs, the energy of the O-2p orbital lies below the d orbital of the transition metal, and the p–d hybridization is weak.[15] By contrast, for late TMOs such as nickelates, resonant inelastic x-ray scattering spectroscopy has revealed abundant oxygen holes in the ground state due to strong p–d hybridization.[16] A negative effective charge-transfer energy Δ' has been suggested, where $\Delta' = \Delta - \frac{W_d + W_p}{2}$, with W_d and W_p denoting the bandwidths of the Ni-3d and O-2p bands, respectively. For a given transition metal, x-ray absorption spectroscopy (XAS) has demonstrated that p–d hybridization increases with the oxidation state, which is understood by a reduced Δ resulting from the reduction of the transition-metal 3d level with respect to the O-2p level.[17,18] These results suggest viable ways to manipulate the p–d hybridization and related properties in TMOs.

†Corresponding author. E-mail: wytong@ee.ecnu.edu.cn

‡Corresponding author. E-mail: bbchen@phy.ecnu.edu.cn

© 2025 Chinese Physical Society and IOP Publishing Ltd. All rights, including for text and data mining, AI training, and similar technologies, are reserved.

Rare-earth nickelates (RNiO$_3$, with R = rare earth) have gained renewed interest due to the discovery of superconductivity in infinite-layer films as well as in Ruddlesden–Popper perovskites under high pressure.[19–21] The RNiO$_3$ family shows a typical bandwidth-controlled metal–insulator transition (MIT) depending on the R size (equivalent to t).[22,23] LaNiO$_3$ (LNO) with $t = 0.94$ is metallic down to the lowest temperature. For smaller R ions, the MIT occurs upon cooling, and the transition temperature consistently increases with decreasing t. Apparently, the more bent Ni–O–Ni bonds at smaller t suppress the hybridization between O-2p and Ni-3d orbitals and reduce the bandwidth, favoring an insulating ground state.[24] Here, we start with LNO, which shows the strongest p–d hybridization among the RNiO$_3$ family. A series of high-quality La$_{1-x}$Ba$_x$NiO$_3$ (LBNO, $0 \leq x \leq 0.25$) single-crystal films were successfully stabilized on (001)-oriented SrTiO$_3$ (STO) substrates using pulsed laser deposition (PLD). Ba^{2+} ions with a radius of $r = 1.35$ Å (significantly larger than the radius of La^{3+}, $r = 1.06$ Å) are intentionally used to dope LNO to further increase t and thus enhance p–d hybridization. Detailed XAS measurements of the oxygen K edge confirm the enhancement in p–d hybridization with increasing Ba doping concentration x. First-principles calculations suggest that Ba doping not only straightens the Ni–O–Ni bond angle by increasing t but also reduces Δ by lowering the on-site energy of Ni 3d compared to the O-2p state. The steric effect of Ba doping is further revealed by comparing the O K edge spectra of Ba-doped LaNiO$_3$ (LBNO) ($x = 0.2$) with La$_{0.8}$Sr$_{0.2}$NiO$_3$ (LSNO) and La$_{0.8}$Ca$_{0.2}$NiO$_3$ (LCNO) at the same hole doping level. With the large p–d hybridization, we further demonstrate enhanced catalytic performance for oxygen evolution in LBNO films compared to the parent LNO film.

2. Experimental details

2.1. Material characterizations

LBNO films were prepared using pulsed laser deposition (PLD), which was *in situ* monitored by reflection high-energy electron diffraction (RHEED). The ceramic targets were ablated with a KrF excimer laser (wavelength $\lambda = 248$ nm). The energy and repetition rate of the laser were set to 550 mJ and 5 Hz, respectively. Deposition was conducted at 600 °C under an oxygen pressure of 10 Pa. Prior to the growth, the STO substrates were etched in a buffered HF (BHF) solution for 23 s, followed by annealing at 1000 °C for 150 min in order to obtain a single terminated surface with clear terraces.

X-ray diffraction (XRD) measurements were performed on a high-resolution PANalytical X'Pert^3 materials research diffractometer with Cu $K_{\alpha 1}$ radiation ($\lambda = 1.5406$ Å). The electrical transport properties were measured on the physical property measurement system (PPMS) using the four-probe method. X-ray absorption spectroscopy (XAS) measurements were carried out in the total electron yield (TEY) mode at the soft x-ray spectroscopy microscopic beamline station at the Shanghai Synchrotron Radiation Facility (SSRF).

2.2. Theoretical details

Our density functional theory (DFT) calculations were performed using the accurate full-potential projector augmented wave method,[25] as implemented in the Vienna *Ab initio* Simulation Package (VASP).[26] The exchange–correlation potential was treated in the Perdew–Burke–Ernzerhof (PBE) form[27] of the generalized gradient approximation with a kinetic energy cutoff of 600 eV. The Brillouin zone was sampled with $7 \times 7 \times 5$ Monkhorst–Pack k-point meshes for the $\sqrt{2} \times \sqrt{2} \times 2$ supercells. The convergence criterion for the electronic energy was 10^{-6} eV and the structures were relaxed until the Hellmann–Feynman force on each atom was less than 1 meV/Å. The in-plane lattice constant was constrained to the optimized STO value ($a = 3.824$ Å). In order to better describe the electronic correlations of the localized Ni-3d electrons, the GGA$+U$ method was adopted.[28] Here, the Coulomb interaction parameter U and exchange interaction parameter J were chosen to be 5.0 eV and 1.0 eV, respectively.[29] The Kohn–Sham eigenvalues of the core level calculated in the initial-state approximation[30] were used to align band structures for the hole-doped case. We determined the average on-site energy of the O-2p and Ni-3d states from the effective Hamiltonian obtained by the wannier90 tool.[31]

2.3. Electrochemical measurements

Electrochemical analysis was carried out using a three-electrode system with a 1 mol/L KOH solution (Bio-Logic VMP3), where Hg/HgO and platinum filaments were used as the reference and counter electrodes, respectively. Linear sweep voltammetry was conducted at a scanning rate of 5 mV/s to assess the oxygen evolution reaction (OER) activity. The reversible hydrogen electrode (RHE) potential was evaluated according to the following equation: $E(\mathrm{RHE}) = E_0 + 0.059 \times \mathrm{pH} + E(\mathrm{SCE})$, where E_0 was 0.098 V, pH = 13.6 for the 1.0 mol/L KOH solution, and $E(\mathrm{SCE})$ was the working voltage (V).

3. Results and discussion

The crystal structure of the LBNO films was first examined by high-resolution XRD. As seen from the XRD linear scans in Fig. 1(a), all films were phase-pure and (00l) single-oriented for $0 \leq x \leq 0.25$. Note that an impurity phase of NiO was detected for $x = 0.3$ (see Fig. S1), probably due to the large difference in ionic radius between La^{3+} and Ba^{2+}. The discussion in this study is limited to $x \leq 0.25$ hereafter. Clear Laue fringes around the film peaks can be observed for

all the films, attesting to their high quality. The film thickness determined from the fringes is around 20 nm. As x increases, the film peak gradually shifts to lower Bragg angles. The out-of-plane lattice constant c is extracted and plotted against x in Fig. 1(b). The c for $x = 0.25$ was determined by fitting the spectrum with the InteractiveXRDFit program (see Fig. S2).[32]

For LNO, c was determined to be 3.79 Å, smaller than the bulk value (3.84 Å) because of the in-plane tensile strain due to STO. Upon doping with Ba, c almost linearly increases with x, which is consistent with the larger size of Ba^{2+} compared to that of La^{3+}. The strain states of LBNO films were evaluated by XRD reciprocal space mapping (RSM) (see Figs. 1(c) and S3). All the films shared the same in-plane Q value as the STO substrate, confirming the coherently strained state. The surface morphology of the film was studied by atomic force microscopy (see Figs. 1(d), 1(e) and S4). Clear terraces with single-unit-cell heights were observed for all films, resembling the prepared STO surface, indicative of a layer-by-layer growth mode. The characterizations suggest that high-quality LBNO films were realized and that Ba^{2+} ions were successfully doped into the LNO lattice.

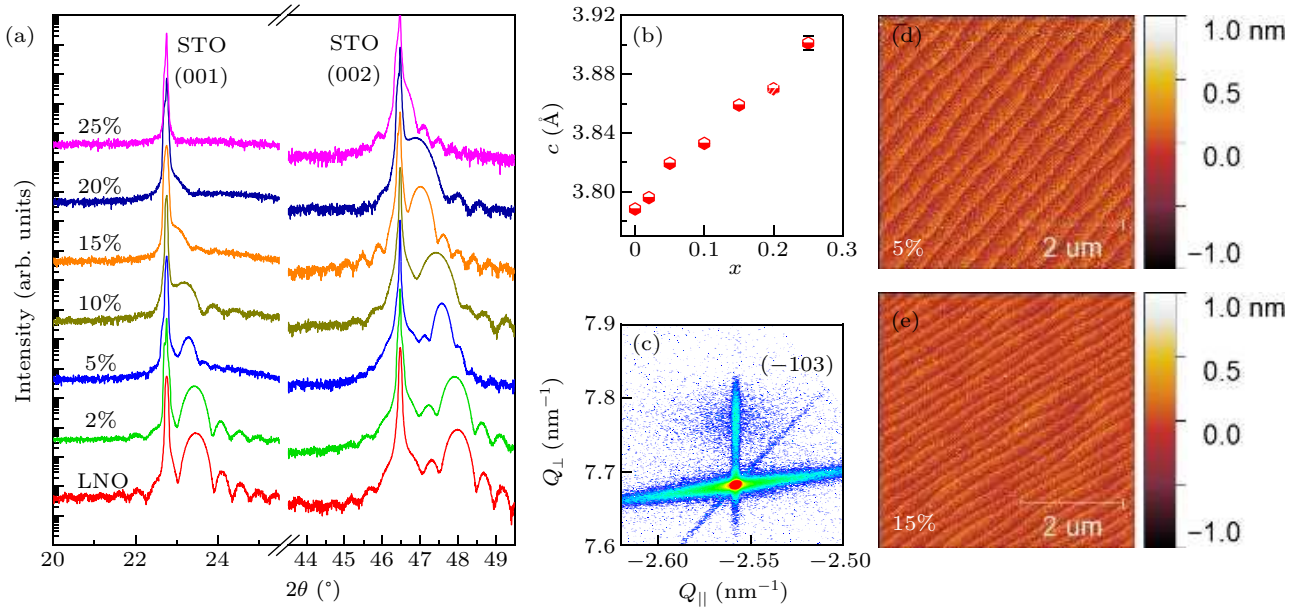


Fig. 1. (a) XRD linear scans showing the regions around the STO (001) and (002) peaks for LBNO films with various Ba doping concentrations x. (b) The out-of-plane lattice constant, c as a function of x. (c) RSM around the (–103) reflection for the $x = 0.15$ film. (d) and (e) AFM images of LBNO films with $x = 0.05$ and 0.15, respectively.

The effects of Ba doping on the electronic structure of LNO were investigated by XAS measurements conducted at the SSRF. Figure 2(a) shows the XAS spectra at the Ni-$L_{2,3}$ thresholds, which characterize excitation from the Ni 2p core level to the 3d states. Each spectrum is normalized to the peak intensity of the La-M_4 edge, which strongly overlaps with the Ni-L_2 edge. Surprisingly, the spectra hardly change as x increases up to 0.25. At first glance, this could be due to the relatively low Ba^{2+} doping level in the LBNO system. Moreover, given the negative Δ' of LNO, the doped holes prefer to occupy oxygen sites instead of Ni sites.[33] This is different from typical Mott insulators, like $LaTiO_3$, where the doped holes primarily occupy the Ti 3d band and the Ti-L edge spectrum changes significantly with doping.[34] We next consider the oxygen K edge spectra, which probe excitation from the oxygen 1s core level to the 2p state. In TMOs, the oxygen 2p states are usually hybridized with the 3d states of the transition metal, and the resultant ligand hole state manifests as a prepeak in the oxygen K edge spectra.[35] As shown in Figs. 2(b) and 2(c), two main changes can be observed in the spectra of LBNO. First, the prepeak shifts to lower energy with increasing x, reaching 200 meV at $x = 0.25$. The decreasing absorption threshold is in agreement with observations of hole-doped $Nd_2NiO_{4-\delta}$[36] and suggests a reduced energy difference between the oxygen 1s core level and the hybridized state of O-2p and Ni-3d. We notice that a systematic shift of the prepeak has been reported in $NdNiO_3$ films subjected to tensile strain, where a comparable energy shift of 270 meV is observed at a strain level of +4%.[37] In LBNO films with various x, the strain effect is overestimated, since all films are coherently strained to the STO substrate and the variation in Ni–O bond length should be minimal. Second, the prepeak broadens as x increases. The full width at half maximum (FWHM) increases from 0.95 eV at $x = 0$ to 1.33 eV at $x = 0.25$. It has been widely recognized that the FWHM of the prepeak is a direct measure of the strength of p–d hybridization.[37,38] Thus, the broadened prepeak suggests enhanced p–d hybridization in LBNO with increasing Ba doping. Figure 2(d) depicts the temperature dependent resistivity curves of the LBNO films. Their resistivity increases with x, and the films remain metal-

lic. The increased resistivity is somewhat in contradiction to the enhanced p–d hybridization in LBNO films with larger x. This discrepancy can be explained by the chemical disorder induced by Ba doping, which introduces extra carrier scattering. The increased disorder effect is reflected in the small resistivity upturn observed at low temperatures for $x \geq 0.15$.

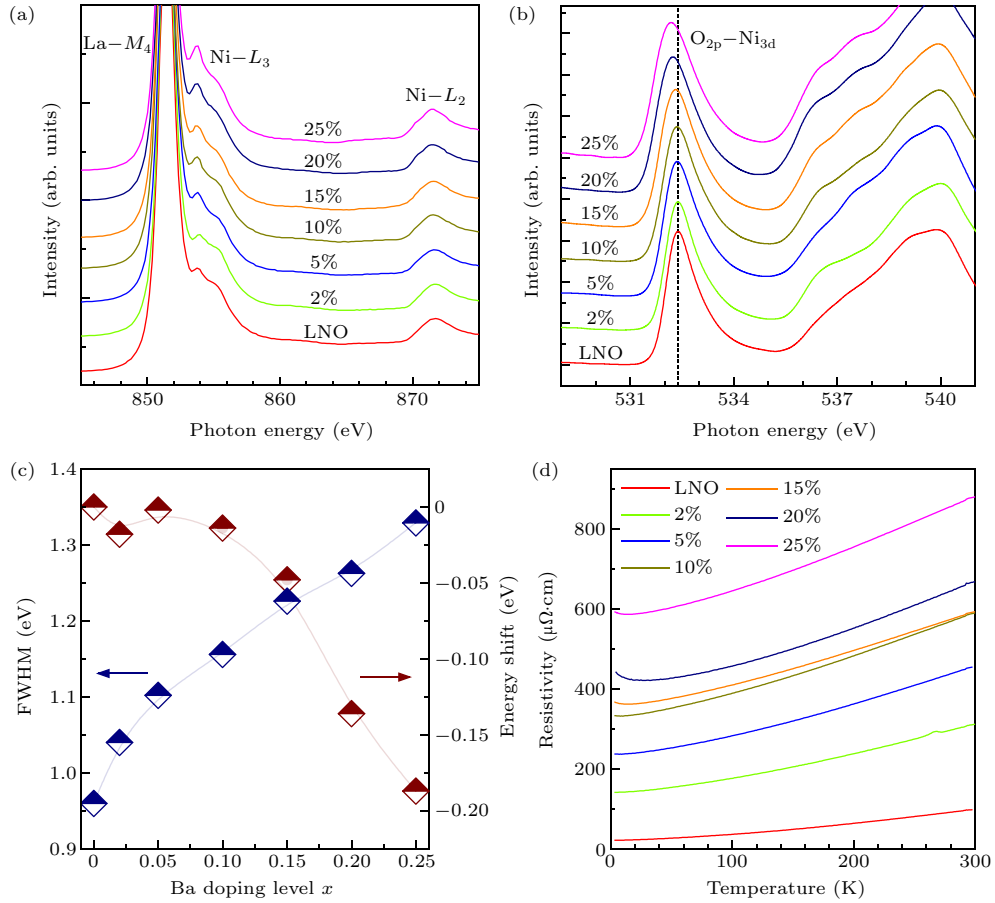


Fig. 2. (a) XAS of Ni $L_{2,3}$ edges measured for LBNO films with various Ba^{2+} doping concentrations x. (b) XAS of the oxygen K edge. The FWHM of the prepeak and the energy shift relative to LNO are extracted and plotted as a function of x in panel (c). (d) Temperature-dependent resistivity curves of LBNO films.

To decipher the origin of enhanced p–d hybridization in LBNO, we further compared LBNO with LSNO and LCNO films that had identical levels of hole doping ($x = 0.2$). Apparently, the doping-induced structural changes are different in the three samples because of the different ionic radii of the dopants, namely, Ba^{2+}(1.35 Å) > Sr^{2+}(1.13 Å) > La^{3+}(1.06 Å) > Ca^{2+}(0.99 Å). The films were prepared with the same deposition parameters to preclude any effects due to extrinsic factors, such as oxygen vacancies. All films show a layer-by-layer growth pattern and are coherently strained to the STO substrates (see Figs. S5 and S6). As shown in Fig. 3(a), the film peak of LCNO shifts slightly to a higher Bragg angle than that of pure LNO, which is indicative of reduced c due to doping with the smaller ions of Ca^{2+}. By contrast, doping with Sr^{2+} and Ba^{2+} results in larger values of c than that of LNO. XAS measurements on the Ni-L edge reveal no discernible changes among LCNO, LSNO, and LBNO (see Fig. S7), which is indicative of the same nominal oxidation state of nickel. Figure 3(b) compares the oxygen K edge XAS for the three films and LNO. The FWHM and the energy shift of the prepeak with respect to LNO are extracted and plotted in Fig 3(c). This shows that the prepeak shifts to a lower energy as a result of hole doping, and the peak shift is more evident for larger dopants. The observation is consistent with the downward shift of the prepeak in LBNO films with increasing x (see Fig. 2(c)). Considering that the LCNO, LSNO, and LBNO samples had the same hole-doping level, the systematic shift of the prepeak can be mainly ascribed to the doping-induced structural modulations. On the other hand, it is surprising to find that LCNO shows stronger hybridization than LNO, even though Ca^{2+} is smaller than La^{3+}. This means that, aside from the structural effect, hole-injection-induced changes in band structure also contribute to the variation of p–d hybridization. Importantly, FWHM significantly increases from $\sim$ 1.13 eV in LCNO and LSNO to $\sim$ 1.3 eV in LBNO. Such an enhancement can only be ascribed to the larger structural modulation induced by Ba^{2+} doping. We compare the transport behavior of the four films in Fig. 3(d). The hole-doped samples show larger resistivity than the parent LNO film due to the increased disorder scattering. Among the three doped films, the

LBNO film shows smaller resistivity than LSNO and LCNO. This means that, in the presence of the same level of disorder, the enhanced p–d hybridization results in higher conductivity for LBNO.

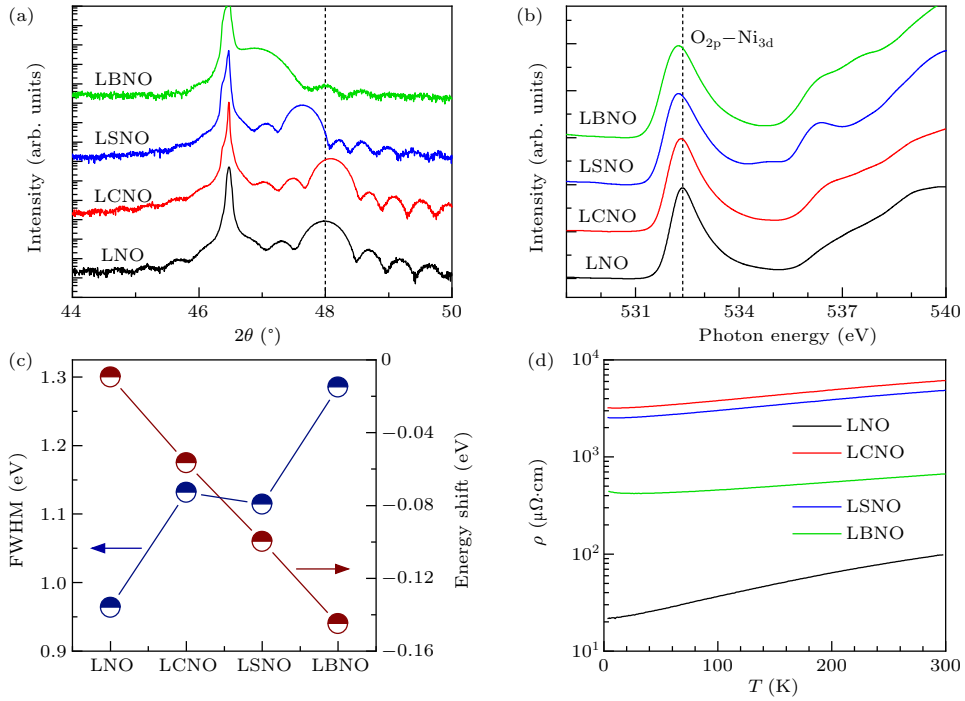


Fig. 3. (a) XRD linear scans of LBNO, LSNO, and LCNO at the same hole doping level ($x = 0.2$). The scan of pure LNO is also shown as a benchmark. (b) O *K* edge XAS measured for the four films. The extracted FWHM and energy shift are plotted in panel (c). (d) Temperature-dependent resistivity curves.

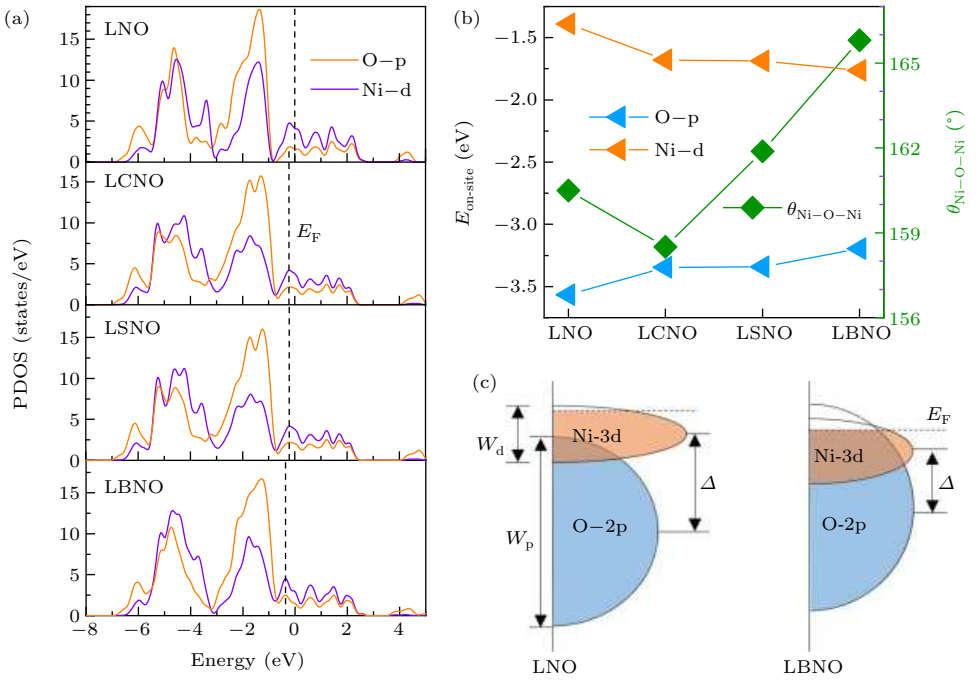


Fig. 4. (a) DOS of the O-2p and Ni-3d states near E_F calculated for LNO, LCNO, LSNO, and LBNO. (b) The on-site energies of the O-2p and Ni-3d states as well as the mean Ni–O–Ni bond angle derived for LNO, LCNO, LSNO, and LBNO. (d) Schematic of the changes in band structure due to Ba^{2+} doping.

First-principles calculations were performed to understand the effect of hole doping on the electronic structures of LNO. Figure 4(a) compares the density of states (DOS) near the Fermi level (E_F) for LNO, LCNO, LSNO, and LBNO. For simplicity, the doping level was set to 25% in the calculation. Compared to LNO, E_F shifts to a lower energy for the hole-doped samples. The overall change of DOS is marginal for different dopants. The on-site energies of O-2p and Ni-3d are plotted in Fig. 4(b). This shows that the on-site energy of Ni-3d is smaller in the hole-doped LNO than in the parent com-

pound LNO. Importantly, as the radius of the dopant increases, the on-site energy of the Ni-3d band decreases, while the on-site energy of the O-2p band shifts to a higher energy. As a result, the charge transfer energy (Δ) decreases with increasing dopant radius, as schematically illustrated in Fig. 4(c). Consequently, the reduced Δ leads to enhanced p–d hybridization in hole-doped LNO. To investigate the doping-induced structural effects, we also calculated the mean Ni–O–Ni bond angle, as plotted in Fig. 4(b). The Ni–O–Ni bond angle decreases from 160.5° in LNO to 158° in LCNO, which is consistent with the decreased t due to the smaller radius of Ca^{2+} ions. Note that XAS measurements suggest stronger p–d hybridization in LCNO than in LNO (see Fig. 3(c)). This means that the effect of a reduced Δ dominates over the effect of the buckling of Ni–O–Ni bonds in LCNO. By contrast, the Ni–O–Ni bond angles increase to 162° and 166° for LSNO and LBNO, respectively. The larger Ni–O–Ni bond angle increases the spatial overlap between the Ni-3d and O-2p orbitals and further enhances their hybridization. Therefore, our first-principles calculations suggest that the strong p–d hybridization in LBNO originates from the joint effects of the reduced Δ and the increased Ni–O–Ni bond angle due to Ba^{2+} doping.

TMOs represent an important class of materials with diverse functionalities. Recently, TMOs have been recognized as promising catalysts for the OER owing to their superior performance and earth abundance.[39] It has been suggested that the OER activity is maximized in TMOs that have strong p–d hybridization and a near-unity occupancy of the transition-metal e_g orbital.[40] This places $RNiO_3$ among the most promising TMO catalysts that fulfill the two design principles. In Figs. 5(a)–5(c), we compare the OER performance of LBNO with those of LNO, LCNO, and LSNO. The potential required to reach a current density of 50 μA/cm^2 is defined as the OER onset potential for TMOs, i.e., the overpotential (η).[40] As can be seen in Figs. 5(b) and 5(c), the parent LNO film shows an overpotential of 0.38 V and a current density of 70 μA/cm^2 at $\eta = 0.4$ V, in good agreement with previous studies.[38,41] Under hole doping, η decreases to $\sim$ 0.36 V for LCNO and LSNO and then to 0.34 V in LBNO. Moreover, the LCNO and LSNO films show comparable current densities of 110 μA/cm^2 and 100 μA/cm^2, which increase to 140 μA/cm^2 in LBNO. These results reveal that the LBNO film has enhanced OER performance, in accordance with the enhanced p–d hybridization shown in Fig. 3(c). During the OER, the reaction intermediates (*OH, *O, *OOH) interact with the surface oxygen of LBNO. The enhanced p–d hybridization in LBNO can facilitate electron transfer between the catalyst and oxygen adsorbates, leading to improved OER activity. Note that the nominal e_g electrons in LNO decrease and deviate from unity due to hole doping, which can suppress OER activity.[38] The enhanced OER performance observed in the hole-doped samples suggests that the enhanced hybridization dominates over the change in e_g electrons at a doping level of 20%. We further compared the OER performance of LBNO films with thicknesses of 10 nm and 30 nm (Fig. S8). XRD measurements indicate a sort of relaxation of the in-plane tensile strain for the 30-nm film. It is found that the OER activity improves with increasing film thickness, manifested by a larger current density for the 30-nm film. Note that the OER catalysis takes place at the surface of the film. Thickness-dependent surface changes should be minimal for the two LBNO films, and the different OER performances can be attributed to the variation in their strain states. The results are supported by the previous study on strain-dependent OER performance in LNO epitaxial films.[41] The in-plane compressive strain tends to favor electron occupation of the Ni-d_{z^2} orbital, which has greater overlap with the O-2p adsorbate orbital, leading to an enhancement in OER activity. On the contrary, the in-plane tensile strain suppresses the OER activity by promoting the Ni-$d_{x^2-y^2}$ orbital occupation. In this regard, strain engineering can be a promising way to further boost the OER performance of LBNO films.

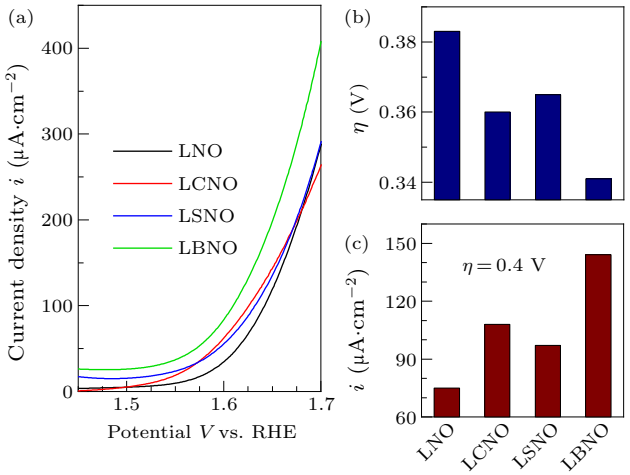


Fig. 5. (a) Linear sweep voltammetry (LSV) curves measured for LNO, LCNO, LSNO, and LBNO. The overpotential (η) and current density at $\eta = 0.4$ V are compared in panels (b) and (c), respectively.

4. Conclusion

In summary, high-quality LBNO films were epitaxially stabilized on STO substrates using PLD. XAS measurements confirmed enhanced p–d hybridization with increasing Ba doping levels. By comparing LBNO with LCNO and LSNO that had the same hole-doping level, we confirmed that the joint effects from the reduced Δ due to hole injection and the straightened Ni–O–Ni bond angle due to increased t give rise to enhanced hybridization in LBNO. We further showed that the enhanced p–d hybridization can be utilized to boost the OER performance of LNO. Therefore, our results shed new insights into the engineering of orbital hybridization in TMOs for enhanced functionalities. Moreover, superconductivity has been recently realized in hole-doped infinite-layer nickelate

films, which show a certain resemblance to the superconducting cuprates.[42] Given the prominent cation effect on the critical temperature in cuprate superconductors,[43] it would be interesting to examine the $La_{1-x}Ba_xNiO_2$ infinite-layer films in a future study, as superconductivity has not yet been addressed in these materials.

Acknowledgments

Project supported by the National Key R&D Program of China (Grant No. 2022YFA1402902), the National Natural Science Foundation of China (Grant Nos. 12374179, 12074119, 12374145, 051B22001, 12104157, 12134003, and 12304218), and the Shanghai Pujiang Program (Grant No. 23PJ1402200).

References

[1] Inoue I H, Goto O, Makino H, Hussey N E and Ishikawa M 1998 *Phys. Rev. B* **58** 4372
[2] Li Y, Cai X, Sun W, Yang J, Guo W, Gu Z, Zhu Y and Nie Y 2023 *Chin. Phys. Lett.* **40** 076801
[3] Hwang H Y, Cheong S W, Radaelli P G, Marezio M and Batlogg B 1995 *Phys. Rev. Lett.* **75** 914
[4] Li J, Chen Y, Gong N, Huang X, Yang Z and Weng Y 2024 *Chin. Phys. B* **33** 017502
[5] Cohen R E 1992 *Nature* **358** 136
[6] Suntivich J, Gasteiger H A, Yabuuchi N, Nakanishi H, Goodenough J B and Shao-Horn Y 2011 *Nature Chemistry* **3** 546
[7] Goldschmidt V M 1926 *Naturwissenschaften* **14** 477
[8] Schlom D G, Chen L Q, Fennie C J, Gopalan V, Muller D A, Pan X, Ramesh R and Uecker R 2014 *MRS Bulletin* **39** 118
[9] Fan Y Y, Wang J, Hu F X, Li B H, Geng A C, Yin Z, Zhang C, Zhou H B, Wang M Q, Yu Z B and Shen B G 2023 *Chin. Phys. B* **32** 087504
[10] Vailionis A, Boschker H, Siemons W, Houwman E P, Blank D H A, Rijnders G and Koster G 2011 *Phys. Rev. B* **83** 064101
[11] Rondinelli J M, May S J and Freeland J W 2012 *MRS Bulletin* **37** 261
[12] Moon E J, Balachandran P V, Kirby B J, Keavney D J, Sichel-Tissot R J, Schlepütz C M, Karapetrova E, Cheng X M, Rondinelli J M and May S J 2014 *Nano Lett.* **14** 2509
[13] Liao Z, Huijben M, Zhong Z, Gauquelin N, Macke S, Green R J, Van Aert S, Verbeeck J, Van Tendeloo G, Held K, Sawatzky G A, Koster G and Rijnders G 2016 *Nat. Mater.* **15** 425
[14] Chen B, Gauquelin N, Green R J, Lee J H, Piamonteze C, Spreitzer M, Jannis D, Verbeeck J, Bibes M, Huijben M, Rijnders G and Koster G 2021 *Nano Lett.* **21** 1295
[15] Grisolia M N, Varignon J, Sanchez-Santolino G, Arora A, Valencia S, Varela M, Abrudan R, Weschke E, Schierle E, Rault J E, Rueff J P, Barthélémy A, Santamaria J and Bibes M 2016 *Nat. Phys.* **12** 484
[16] Bisogni V, Catalano S, Green R J, Gibert M, Scherwitzl R, Huang Y, Strocov V N, Zubko P, Balandeh S, Triscone J M, Sawatzky G and Schmitt T 2016 *Nat. Commun.* **7** 13017
[17] Suntivich J, Hong W T, Lee Y L, Rondinelli J M, Yang W, Goodenough J B, Dabrowski B, Freeland J W and Shao-Horn Y 2014 *The Journal of Physical Chemistry C* **118** 1856
[18] Bocquet A E, Mizokawa T, Saitoh T, Namatame H and Fujimori A 1992 *Phys. Rev. B* **46** 3771
[19] Li D, Lee K, Wang B Y, Osada M, Crossley S, Lee H R, Cui Y, Hikita Y and Hwang H Y 2019 *Nature* **572** 624
[20] Sun H, Huo M, Hu X, Li J, Liu Z, Han Y, Tang L, Mao Z, Yang P, Wang B, Cheng J, Yao D X, Zhang G M and Wang M 2023 *Nature* **621** 493
[21] Zhu Y, Peng D, Zhang E, Pan B, Chen X, Chen L, Ren H, Liu F, Hao Y, Li N, Xing Z, Lan F, Han J, Wang J, Jia D, Wo H, Gu Y, Gu Y, Ji L, Wang W, Gou H, Shen Y, Ying T, Chen X, Yang W, Cao H, Zheng C, Zeng Q, Guo J G and Zhao J 2024 *Nature* **631** 531
[22] Catalan G 2008 *Phase Transitions* **81** 729
[23] Catalano S, Gibert M, Fowlie J, Íñiguez J, Triscone J M and Kreisel J 2018 *Reports on Progress in Physics* **81** 046501
[24] Torrance J B, Lacorre P, Nazzal A I, Ansaldo E J and Niedermayer C 1992 *Phys. Rev. B* **45** 8209
[25] Blöchl P E 1994 *Phys. Rev. B* **50** 17953
[26] Kresse G and Joubert D 1999 *Phys. Rev. B* **59** 1758
[27] Perdew J P, Burke K and Ernzerhof M 1996 *Phys. Rev. Lett.* **77** 3865
[28] Dudarev S L, Botton G A, Savrasov S Y, Humphreys C J and Sutton A P 1998 *Phys. Rev. B* **57** 1505
[29] Golalikhani M, Lei Q, Chandrasena R U, Kasaei L, Park H, Bai J, Orgiani P, Ciston J, Sterbinsky G E, Arena D A, Shafer P, Arenholz E, Davidson B A, Millis A J, Gray A X and Xi X X 2018 *Nat. Commun.* **9** 2206
[30] Köhler L and Kresse G 2004 *Phys. Rev. B* **70** 165405
[31] Pizzi G, Vitale V, Arita R, Blügel S, Freimuth F, Géranton G, Gibertini M, Gresch D, Johnson C, Koretsune T, Ibañez-Azpiroz J, Lee H, Lihm J M, Marchand D, Marrazzo A, Mokrousov Y, Mustafa J I, Nohara Y, Nomura Y, Paulatto L, Poncé S, Ponweiser T, Qiao J, Thöle F, Tsirkin S S, Wierzbowska M, Marzari N, Vanderbilt D, Souza I, Mostofi A A and Yates J R 2020 *J. Phys.: Condens. Matter* **32** 165902
[32] Lichtensteiger C 2018 *Journal of Applied Crystallography* **51** 1745
[33] Kuiper P, Kruizinga G, Ghijsen J, Sawatzky G A and Verweij H 1989 *PPhys. Rev. Lett.* **62** 221
[34] Abbate M, de Groot F M F, Fuggle J C, Fujimori A, Tokura Y, Fujishima Y, Strebel O, Domke M, Kaindl G, van Elp J, Thole B T, Sawatzky G A, Sacchi M and Tsuda N 1991 *Phys. Rev. B* **44** 5419
[35] de Groot F M F, Grioni M, Fuggle J C, Ghijsen J, Sawatzky G A and Petersen H 1989 *Phys. Rev. B* **40** 5715
[36] Hu Z, Golden M S, Fink J, Kaindl G, Warda S A, Reinen D, Mahadevan P and Sarma D D 2000 *Phys. Rev. B* **61** 3739
[37] Liu J, Kargarian M, Kareev M, Gray B, Ryan P J, Cruz A, Tahir N, Chuang Y D, Guo J, Rondinelli J M, Freeland J W, Fiete G A and Chakhalian J 2013 *Nat. Commun.* **4** 2714
[38] Liu J, Jia E, Wang L, Stoerzinger K A, Zhou H, Tang C S, Yin X, He X, Bousquet E, Bowden M E, Wee A T S, Chambers S A and Du Y 2019 *Advanced Science* **6** 1901073
[39] Hwang J, Rao R R, Giordano L, Katayama Y, Yu Y and Shao-Horn Y 2017 *Science* **358** 751
[40] Suntivich J, May K J, Gasteiger H A, Goodenough J B and Shao-Horn Y 2011 *Science* **334** 1383
[41] Petrie J R, Cooper V R, Freeland J W, Meyer T L, Zhang Z, Lutterman D A and Lee H N 2016 *J. Am. Chem. Soc.* **138** 2488
[42] Wang B Y, Lee K and Goodge B H 2024 *Ann. Rev. Condensed Matter Phys.* **15** 305
[43] Attfield J P, Kharlanov A L and McAllister J A 1998 *Nature* **394** 157